

## Regularized shock solutions in coating flows with small surface tension

D. Badali,<sup>1</sup> M. Chugunova,<sup>2</sup> D. E. Pelinovsky,<sup>3</sup> and S. Pollack<sup>4</sup>

<sup>1</sup>*Department of Chemical and Physical Science, University of Toronto at Mississauga, Mississauga, Ontario L5L 1C6, Canada*

<sup>2</sup>*Department of Mathematics, University of Toronto, Toronto, Ontario M5S 1A1, Canada*

<sup>3</sup>*Department of Mathematics, McMaster University, Hamilton, Ontario L8S 4K1, Canada*

<sup>4</sup>*Department of Mathematics, McGill University, Montreal, Quebec H3A 2T5, Canada*

(Received 4 January 2011; accepted 22 July 2011; published online 20 September 2011)

We study the dynamics of thin liquid films on the surface of a rotating horizontal cylinder in the presence of gravity in the small surface tension limit. Using dynamical system methods, we show that the continuum of shock solutions increasing across the jump point persists in the small surface tension limit, whereas the continuum of shock solutions decreasing across the jump point terminates in the limit. Using delicate numerical computations, we show that the number of steady states with equal mass increases as the surface tension parameter goes to zero. This corresponds to an increase in the number of loops on the mass-flux bifurcation diagram. If  $n$  is the number of loops in the mass-flux diagram with  $2n + 1$  solution branches, we show that  $n + 1$  solution branches are stable with respect to small perturbations in the time evolution of the liquid film. © 2011 American Institute of Physics. [doi:10.1063/1.3635535]

### I. INTRODUCTION

The time evolution of a liquid film spreading over a solid surface under the action of the surface tension and viscosity can be described by lubrication models.<sup>1–5</sup> These models approximate the full system of Navier-Stokes equations that describe the motion of the liquid films. Thin films play an increasingly important role in a wide range of applications, for example, packaging, barriers, membranes, sensors, semiconductor devices, and medical implants.<sup>6–8</sup>

We are concerned here with the dynamics of a viscous incompressible thin fluid film on the outer surface of a horizontal circular cylinder that is rotating around its axis in the presence of a gravitational field. The rotating thin fluid film can exhibit a variety of different behaviors including pattern formations (“shark teeth” and “duck bill” patterns), fluid curtains, hydroplaning drops, and frontal avalanches.<sup>9,10</sup> As a result, the coating flow has been the subject of continuous study since the pioneering work of Moffatt<sup>11</sup> and Pukhnachov.<sup>12</sup> During the past decade, this problem attracted many researchers who analyzed different types of flow regime asymptotically<sup>13–19</sup> and numerically.<sup>20–22</sup>

The coating flow is generated due to the cylinder’s surface motion relative to the fluid. If the cylinder is fully coated, there is only one free boundary where the liquid meets the surrounding air. Otherwise, there is also a free boundary (or three-phase contact line) where the air and liquid meet the cylinder’s surface. The motion of the liquid film is governed by four physical effects: viscosity, gravity, surface tension, and centrifugal forces.

We can model the flow on a rotating cylinder using the full Navier-Stokes equations for the velocity vector  $\vec{u}(r, \theta, z, t)$ , where  $r$  is the axial variable,  $\theta$  is the angular variable, and  $z$  is the variable in the direction of the cylinder. Let  $h(\theta, t)$  be the thickness of the fluid on the surface of the cylinder at time  $t$ . We shall consider the limit when the average

thickness of the liquid is much smaller than the radius of the cylinder. A model that takes into account small surface tension and gravitational force was considered in a number of works including Pukhnachov<sup>12</sup> and O’Brien.<sup>23</sup> This model is written in the form,

$$\partial_t h + \partial_\theta \left[ h - \frac{1}{3} h^3 \cos(\theta) \right] + \frac{1}{3} \epsilon \partial_\theta [h^3 (\partial_\theta h + \partial_\theta^3 h)] = 0, \quad (1.1)$$

where  $h(\theta + 2\pi, t) = h(\theta, t)$  and  $\epsilon > 0$  is a small parameter. The model (1.1) uses no-slip boundary conditions at the liquid/solid interface. A solution to this model is physically relevant if either  $h$  is strictly positive (the cylinder is fully coated) or  $h$  is nonnegative (the cylinder is dry in some places). Because of slow rotation, the same model describes both the rimming flow (on the inner side of the cylinder) and the coating flow (on the outer side of the cylinder).

The stationary solutions of the model equation (1.1) are given by the  $2\pi$ -periodic solutions of the third-order differential equation,

$$h - \frac{1}{3} h^3 \cos(\theta) + \frac{1}{3} \epsilon h^3 (\partial_\theta h + \partial_\theta^3 h) = Q, \quad (1.2)$$

where  $Q$  is the constant that corresponds physically to flux of the liquid through the film cross section.

A number of researchers including Moffatt,<sup>11</sup> Johnson,<sup>24</sup> Benjamin *et al.*,<sup>25</sup> Wilson and Williams,<sup>26</sup> and O’Brien and Gath<sup>27</sup> considered stationary solutions of Eq. (1.2) with  $\epsilon = 0$ . Besides smooth periodic solutions for  $Q < Q_c = \frac{2}{3}$ , there are two continua of shock solutions for  $Q = Q_c$ , one is associated with the increasing functions at the jump point (called increasing shocks) and the other one is associated with the decreasing functions at the jump point (called decreasing shocks). Both families of solutions are parameterized by the integral,

$$M = \frac{1}{2\pi} \int_{-\pi}^{\pi} h(\theta) d\theta, \tag{1.3}$$

which is the leading-order approximation to the volume of liquid in the cylindrical tube that determines the mass of the liquid. The solution branches can be plotted on the parameter plane  $(M, Q)$  for a fixed value of  $\epsilon$ , which we term as the *mass-flux diagram*.

Previous authors discussed the possibility of decreasing shocks but discarded them physically on the grounds that these shocks are unstable if the surface tension effects are included with  $\epsilon \neq 0$ . Singular perturbation theory of small  $\epsilon$  was recently considered by Benilov *et al.*,<sup>28</sup> where the authors showed by using asymptotic and numerical methods that decreasing shocks do not exist for small positive  $\epsilon$ . On the other hand, increasing shocks exist for small positive  $\epsilon$ , and asymptotic arguments complemented by the numerical approximations were used to predict the linearized stability of increasing shocks.

Pukhnachov<sup>29</sup> proved the existence and uniqueness of the steady states in the differential equation (1.2), if  $\epsilon$  and  $Q$  are small. Karabut<sup>30</sup> constructed two branches of steady states in the limit of large  $\epsilon$ . Numerical approximations in Benilov *et al.*<sup>31</sup> (Figure 14) showed that the mass-flux diagram may become more complicated for small  $\epsilon$  and large  $M$  and may include a loop near the value  $Q = Q_c$ . Three solutions coexist for a fixed  $M$  if the loop is present. Stability of these solutions was not studied in Ref. 31.

It is the purpose of this work to continue, improve, and clarify the results of Benilov *et al.*<sup>28,31</sup> In particular, we use dynamical system methods to prove that the family of increasing shocks persists with respect to  $\epsilon \neq 0$ , whereas the family of decreasing shocks terminates at  $\epsilon = 0$ . This corresponds to the main conclusion of Ref. 28 but relies now on more rigorous geometric theory.

We develop a delicate numerical approximation of the steady solutions of Eq. (1.2) to show that the number of loops on the mass-flux diagram increases when  $\epsilon$  is reduced to zero and the location of these loops goes to infinity. We also apply numerical approximations of eigenvalues of the linearized time evolution associated with the model equation (1.1) and show that if  $n$  is the number of loops on the mass-flux diagram, then  $n + 1$  solution branches are stable with respect to small perturbations. These results give a complete solution of the existence and stability of regularized shock solutions, compared to the numerical computations in Ref. 31.

The paper is organized as follows. Section II presents geometric theory of persistence of increasing shocks. Section III presents numerical results on multi-valued loops in the mass-flux bifurcation diagram. Section IV provides a summary and discusses open questions.

**II. GEOMETRIC THEORY OF REGULARIZED SHOCKS**

We shall study here shock solutions of the steady-state equation (1.2) in the limit of small  $\epsilon$ . The steady-state equation (1.2) can be written in the form,

$$\epsilon \left[ \frac{d^3 h}{d\theta^3} + \frac{dh}{d\theta} \right] = \cos(\theta) - \frac{3(h - Q)}{h^3}, \quad \theta \in (-\pi, \pi). \tag{2.1}$$

We review the limiting solutions at  $\epsilon = 0$  that exist for any  $Q \in (0, \frac{2}{3})$  and prove using a geometric theory that increasing shocks at  $\epsilon = 0$  and  $Q = \frac{2}{3}$  persist for any  $\epsilon > 0$ , whereas decreasing shocks terminate at  $\epsilon = 0$  and do not exist for  $\epsilon > 0$ . The same conclusion was obtained recently<sup>28</sup> using methods involving asymptotic expansions and numerical approximations.

Solutions of the limiting problem at  $\epsilon = 0$ ,

$$F_Q(h) := \frac{3(h - Q)}{h^3} = \cos(\theta), \quad \theta \in (-\pi, \pi), \tag{2.2}$$

depend on the value of the flux  $Q > 0$ .

If  $Q \in (0, \frac{2}{3})$ , the  $2\pi$ -periodic solution  $h(\theta)$  is unique.<sup>11</sup> To obtain this result, we denote the smallest roots of  $F_Q(h) = \pm 1$  for  $Q \in (0, \frac{2}{3})$  by  $h_{\pm}$  such that  $h_- < h_+$  (Figure 1, left). The unique solution of the limiting problem (2.2) satisfies

$$h(-\theta) = h(\theta) : \quad h'(\theta) > 0, \quad \theta \in (-\pi, 0), \tag{2.3}$$

with  $h(\pm\pi) = h_-$ ,  $h(0) = h_+$ , and  $h'(\pm\pi) = h'(0) = 0$ . The unique solution with properties (2.3) is shown in Figure 1 (right top panel) for  $Q = 0.5$ .

If  $Q > \frac{2}{3}$ , no solution  $h(\theta)$  exists because  $\max_{h \in \mathbb{R}_+} F_Q(h) < 1$ .

If  $Q = Q_* = \frac{2}{3}$ , there is a unique continuous solution  $h(\theta)$  with properties (2.3) and  $h(\pm\pi) = h_-$ ,  $h(0) = h_+ \equiv 1$ ,  $h'(-\pi) = 0$ , and  $\lim_{\theta \rightarrow -0} h'(\theta) = \frac{1}{\sqrt{6}}$ . This solution with the sharp corner is shown in Figure 1 (right middle panel) for  $Q = Q_*$ .

Besides the continuous solution with the sharp corner at  $Q = Q_* = \frac{2}{3}$ , there exist two symmetric families of shock solutions with a jump discontinuity at either  $\theta = \theta_0$  or  $\theta = -\theta_0$ , where  $\theta_0 \in (0, \frac{\pi}{2})$  is a continuous parameter.

To construct the shock solutions, we denote the two simple zeros of  $F_{Q_*}(h) = \cos(\theta_0) \in (0, 1)$  by  $H_{\pm}$  such that  $H_- < 1 < H_+$ . The increasing shock is centered at  $\theta = -\theta_0$  and satisfies

$$h'(\theta) > 0, \quad \theta \in (-\pi, -\theta_0), \quad h'(\theta) < 0, \quad \theta \in (-\theta_0, \pi), \tag{2.4}$$

with  $h(\pm\pi) = h_-$ ,  $\lim_{\theta \rightarrow -\theta_0-0} h(\theta) = H_-$ ,  $\lim_{\theta \rightarrow -\theta_0+0} h(\theta) = H_+$ , and  $h'(\pm\pi) = 0$ . The increasing shock is shown in Figure 1 (right bottom panel) for  $Q = Q_*$ . Using the symmetry of the limiting problem (2.2) with respect to reflection  $\theta \rightarrow -\theta$ , the decreasing shock can be constructed using the reflection. It is then centered at  $\theta = \theta_0$ .

The net mass  $M$  defined by Eq. (1.3) is a one-to-one increasing function of  $Q$  for  $Q \in (0, Q_*)$  with  $\lim_{Q \rightarrow 0} M = 0$  and

$\lim_{Q \rightarrow Q_*-0} M = M_*$  for some  $M_* < \infty$ , whereas the two families of shock solutions for  $Q = Q_*$  correspond to the values of  $M \in (M_*, \infty)$ .

To consider the persistence of the two shock solutions with respect to parameter  $\epsilon$ , we shall rescale the coordinate  $\theta$  near  $\pm\theta_0$  by the transformation,

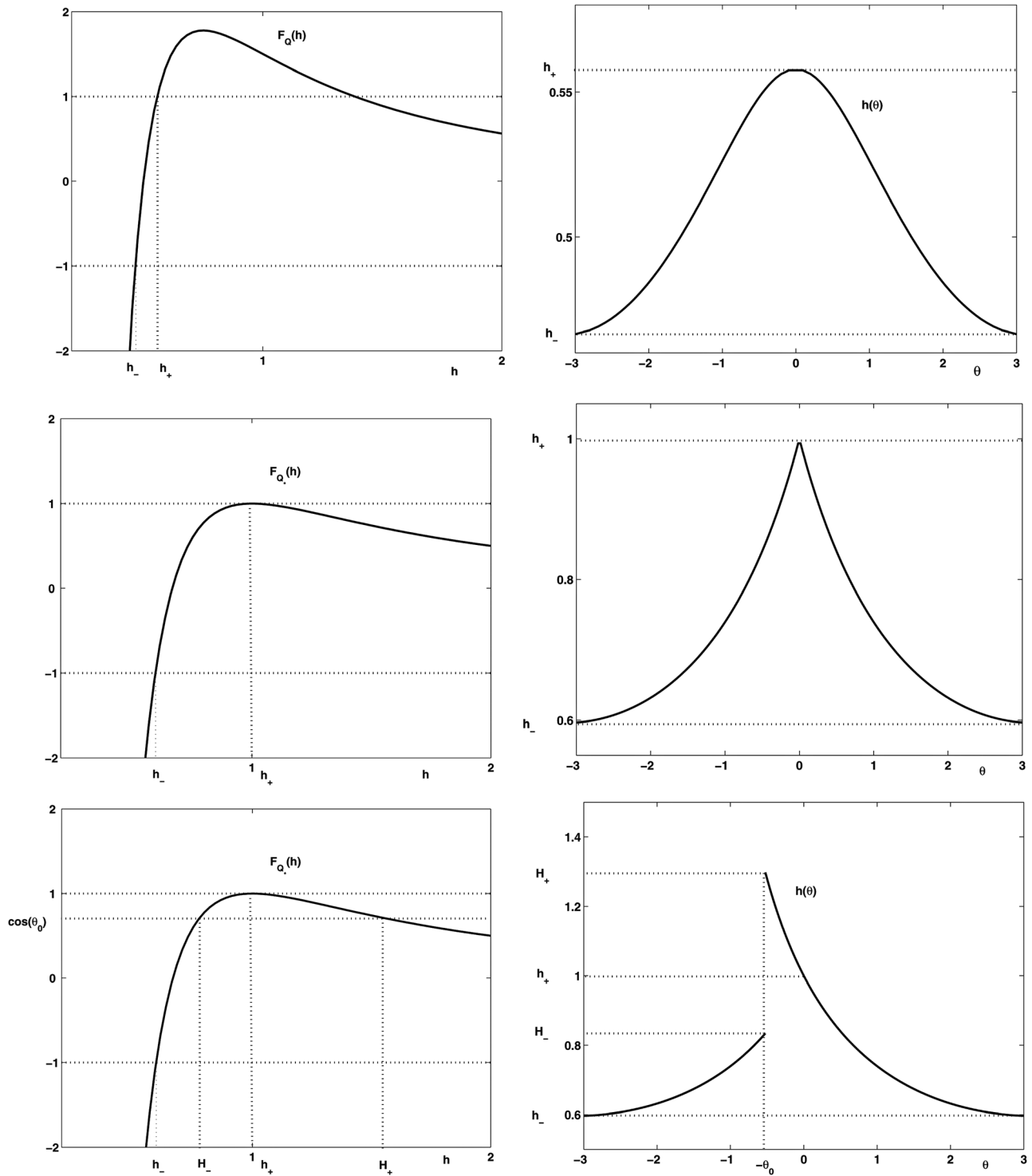


FIG. 1. Function  $F_Q(h)$  (left) and steady-state solution  $h(\theta)$  (right) for  $Q=0.5$  (top) and  $Q=2/3$  (middle and bottom). The right bottom panel shows an increasing shock solution located at  $\theta = -\theta_0$ .

$$h(\theta) = H(x), \quad x = \frac{\theta \mp \theta_0}{\epsilon^{1/3}}. \tag{2.5}$$

The new function  $H(x)$  satisfies a new version of the third-order differential equation, also known as the inner equation,

$$\frac{d^3 H}{dx^3} + \epsilon^{2/3} \frac{dH}{dx} = \cos(\pm\theta_0 + \epsilon^{1/3}x) - F(H), \tag{2.6}$$

$$x \in \left( \frac{-\pi \mp \theta_0}{\epsilon^{1/3}}, \frac{\pi \mp \theta_0}{\epsilon^{1/3}} \right),$$

where  $H(x)$  is a periodic function with period  $2\pi\epsilon^{-1/3}$  and

$$F(H) = F_{Q_*}(H) = \frac{3H - 2}{H^3}.$$

The limiting problem at  $\epsilon = 0$  becomes now the autonomous equation,

$$\frac{d^3 H_0}{dx^3} = \cos(\theta_0) - F(H_0), \quad x \in \mathbb{R}, \tag{2.7}$$

which is posed in the phase space  $(H_0, H'_0, H''_0) \in \mathbb{R}^3$ . Critical points of the dynamical system (2.7) corresponds to zeros of  $F(H_0) = \cos(\theta_0)$ , which are denoted above by  $H_-$  and  $H_+$  such that  $H_- < H_+$ . Solutions of Eq. (2.7) are not available in the closed form; therefore, we shall use dynamical system methods (geometric theory) to analyze shock solutions (heteroclinic orbits). Note in passing that solutions of a simplified version of Eq. (2.7),  $y''' = y^{-2}$  are available in the closed form.<sup>32</sup>

The increasing shock  $h(\theta)$  of the original equation (2.1) corresponds after scaling (2.5) and the limit  $\epsilon \rightarrow 0$  to a heteroclinic orbit  $H_0(x)$  of the reduced equation (2.7) satisfying the boundary conditions,

$$\lim_{x \rightarrow \pm\infty} H_0(x) = H_{\pm}. \quad (2.8)$$

The decreasing shock corresponds to a heteroclinic orbit with the boundary conditions,

$$\lim_{x \rightarrow \pm\infty} H_0(x) = H_{\mp}. \quad (2.9)$$

Linearization of the limiting equation (2.7) near the equilibrium states  $H_{\pm}$  with  $H_0 = H_{\pm} + \tilde{H}_{\pm}(x)$  gives

$$\frac{d^3 \tilde{H}_{\pm}}{dx^3} = -F'(H_{\pm}) \tilde{H}_{\pm}, \quad (2.10)$$

where  $F'(H_-) > 0$  and  $F'(H_+) < 0$ .

If  $F'(H_-) > 0$ , there exist one decaying and two growing solutions of Eq. (2.10) for  $\tilde{H}_-$ . From a geometric point of view, this means that the phase space  $\mathbb{R}^3$  near  $(H_-, 0, 0)$  can be decomposed into the sum of two invariant manifolds, a *two-dimensional* unstable manifold  $W^u(H_-)$  and a *one-dimensional* stable manifold  $W^s(H_-)$ .

Similarly, if  $F'(H_+) < 0$ , there exist two decaying and one growing solutions of Eq. (2.10) for  $\tilde{H}_+$ , hence, the phase space  $\mathbb{R}^3$  near  $(H_+, 0, 0)$  can be decomposed into the sum of two invariant manifolds, a *one-dimensional* unstable manifold  $W^u(H_+)$  and a *two-dimensional* stable manifold  $W^s(H_+)$ .

Here, stable and unstable manifolds are introduced with respect to the flow of the dynamical system (2.7) and they are not related to physical stability of the equilibrium states or shock solutions. Heteroclinic orbits satisfying boundary conditions (2.8) and (2.9), if they exist, are intersections of stable and unstable manifolds from the two critical points  $(H_-, 0, 0)$  and  $(H_+, 0, 0)$  in the phase space  $\mathbb{R}^3$ .

Intersection of two-dimensional manifolds in  $W^u(H_-) \cap W^s(H_+)$  is transverse in the three-dimensional space. Hence, a heteroclinic orbit satisfying the boundary conditions (2.8) exists generally and persists under the perturbation. This heteroclinic orbit corresponds to the increasing shock in the inner equation (2.6).

Intersection of one-dimensional manifolds in  $W^u(H_+) \cap W^s(H_-)$  is non-transverse in the three-dimensional space. Hence, a heteroclinic orbit satisfying the boundary conditions (2.9) does not exist generally and does not persist under the perturbation. Moreover, it was shown in Ref. 28 using sign-definite integral quantities that no solution of the limiting equation (2.7) with the boundary conditions (2.9) exists.

Since the boundary conditions (2.9) correspond to decreasing shocks, we conclude that no decreasing shocks may exist in the inner equation (2.6) for small and zero values of  $\epsilon$ .

Based on this geometric theory of dynamical systems, we summarize that the increasing shock centered at  $\theta = -\theta_0$  persists as a smooth solution  $h(\theta)$  of the third-order equation (2.1) for any small  $\epsilon > 0$ , whereas the decreasing shock centered at  $\theta = \theta_0$  does not persist in the third-order equation (2.1) for any small  $\epsilon > 0$ . This conclusion holds for any fixed  $M > M_*$ . It does not exclude, however, a possibility of a complicated branching behavior in the solutions of the third-order equation (2.1), which can come from  $M = \infty$  for small values of  $\epsilon > 0$ . The limit  $M \rightarrow \infty$  corresponds to the case of large  $h$  and is beyond the applicability of the underlying model (2.1). Nevertheless, as we will show in the next section, bifurcation from  $M = \infty$  at  $\epsilon = 0$  corresponds to non-trivial steady-state solutions, which reside for finite values of  $M$  if  $\epsilon > 0$ .

### III. NUMERICAL APPROXIMATIONS OF REGULARIZED SHOCKS

We shall construct numerical approximations of solutions of the third-order differential equation (2.1). The numerical approximations were generated using a custom-written turning-point algorithm and implemented in MATLAB. Solutions were found using Newton-Raphson iterations and Fourier spectral differentiation matrices with 256, 512, and 1024 Fourier modes. The mass-flux diagram was generated with parameter continuation of  $Q$  or  $M$ , as decided by the algorithm. A convergent solution was defined numerically if the  $(n+1)$ -th iteration  $h_{n+1}(\theta)$  satisfied

$$\sup_{\theta \in [-\pi, \pi]} |h_{n+1}(\theta) - h_n(\theta)| \leq 5 \times 10^{-8}.$$

Eventually, non-convergent solutions were found and the parameter continuation failed at the turning (bifurcation) points. To resolve the mass-flux diagram near the turning point, the following algorithm was implemented: first, a reference point was identified in  $k$  steps behind the turning point (for our simulations, we generally chose  $k=5$ ). Next, the convergence of the algorithm at the points making up a half-circle centered at the turning point was checked. The orientation of the half-circle was chosen to be facing away from the direction of the current parametrization (i.e., if we are increasing along the vertical axis, then the lower half of the circle would be chosen). A vector was then drawn from the turning point to the convergent point with the largest distance from the reference point. Finally, the direction of new parametrization was chosen from the largest component of this vector. We found that this algorithm successfully navigated the loops in the mass-flux diagram.

Figure 2 shows the mass-flux diagram of stationary solutions for four values of  $\epsilon$ . For  $\epsilon = 0.005$  (dashed curve), we see no loops in the mass-flux diagram. For each fixed value of mass  $M$ , there is exactly one value of the flux  $Q$  for the steady states of Eq. (2.1). The first loop is seen for  $\epsilon = 0.001$  (light gray). In an interval of values of  $M$ , three stationary

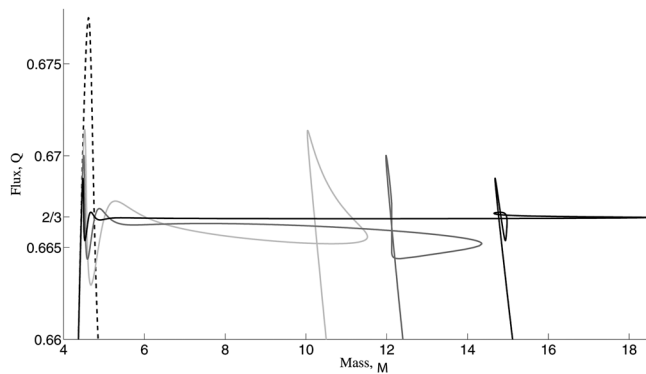


FIG. 2. The mass ( $M$ ) versus the flux ( $Q$ ) of the steady state solutions for various values of  $\epsilon$ : 0.005 (dashed), 0.001 (light gray), 0.0005 (dark gray), and 0.0001 (black).

solutions coexist for three different values of  $Q$ . Note that this loop was discovered by Benilov *et al.*<sup>31</sup> (Figure 14).

Reducing  $\epsilon$  further, we observe a formation and persistence of the second loop in the mass-flux diagram for  $\epsilon = 0.0005$  (dark gray) and  $\epsilon = 0.0001$  (solid black). Five solutions for different values of  $Q$  coexist in an interval of values of  $M$ . The number of loops keeps increasing as  $\epsilon$  decreases to zero and their location is drifted to large values of  $M$ . Figure 3 shows the number of steady states for fixed  $Q = 2/3$  as the value of  $\epsilon$  decreases.

As  $\epsilon \rightarrow 0$ , the mass-flux diagram represents an increasing curve for  $M \in (0, M_*)$  and a constant level  $Q = Q_*$  for  $M > M_*$ , where  $Q_* = \frac{2}{3}$  and  $M_* \approx 4.44272$ . The limiting picture corresponds to the mass-flux diagram of the solutions of the limiting equation (2.2), which include the smooth solutions for  $Q < Q_*$  and the shock solutions for  $Q = Q_*$ .

We focus now on two particular examples of the mass-flux diagram with a single loop and a double loop. Figure 4 (top) shows the mass-flux diagram for  $\epsilon = 0.001$  with a single loop. We can identify three solution branches (labeled as S1, S2, and S3) connected at two bifurcation points (labeled as BF1 and BF2). The other point of intersections of solution branches S1 and S2 is not a bifurcation point, because, the two solutions for the same value of  $M$  and  $Q$  remain distinguishable into two different solutions. For  $M = 10.5$ , we compute the solution profiles and show them in Figure 4

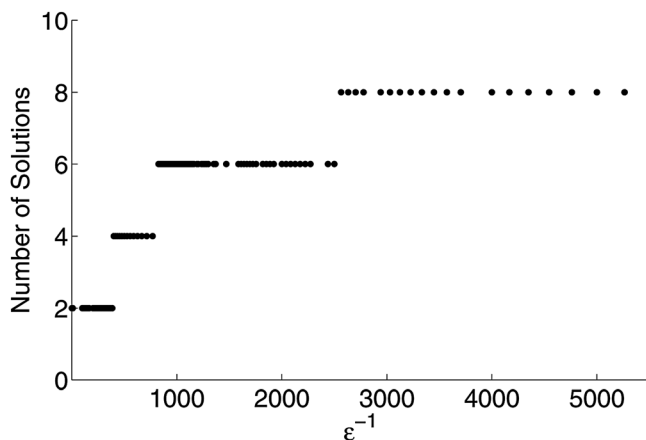


FIG. 3. The number of steady state solutions for  $Q = 2/3$  versus  $\epsilon^{-1}$ .

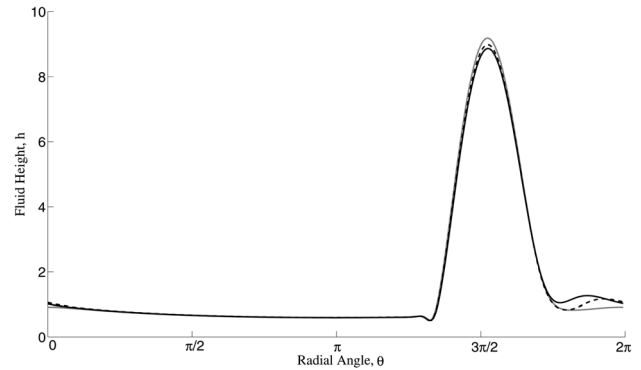
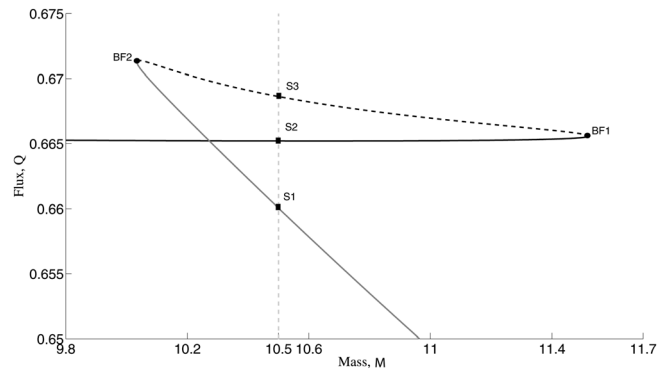


FIG. 4. (Top) A segment of the mass-flux diagram for  $\epsilon = 0.001$ . Three branches are indicated between two bifurcation points (labeled BF1 and BF2). The three branches are shown by solid gray line (S1), solid black line (S2), and dashed line (S3). The dashed gray line shows the value of mass  $M = 10.5$ . (Bottom) Three steady state solutions with  $M = 10.5$  and  $\epsilon = 0.001$ : S1 (solid gray line,  $Q = 0.6601$ ), S2 (solid black line,  $Q = 0.6652$ ), and S3 (dashed line,  $Q = 0.6686$ ).

(bottom). Although similar in their shapes, the three steady state solutions are clearly distinct. The peaks of the solutions are located for  $\theta > \pi$ , or equivalently for  $\theta < 0$ , thanks to the  $2\pi$ -periodicity of the solutions. They correspond to the increasing shock solution as  $\epsilon \rightarrow 0$  located at  $\theta = -\theta_0 < 0$ . Oscillations which are visible on both sides of the shock are attributed to complex eigenvalues of the linearized equation (2.10) after the scaling transformation (2.5) and the limit  $\epsilon \rightarrow 0$ .

Because of multiple steady-state solutions with the same physical parameter of the mass  $M$ , we anticipate that they may have different stability properties. Therefore, we examine eigenvalues of the linearized equation,

$$\lambda f + \partial_\theta [f - h^2 \cos(\theta)f + \epsilon h^2 (\partial_\theta h + \partial_\theta^3 h)f + \frac{1}{3} \epsilon h^3 (\partial_\theta f + \partial_\theta^3 f)] = 0, \tag{3.1}$$

where  $h(\theta)$  is a  $2\pi$ -periodic steady-state solution and  $f(\theta)$  is a  $2\pi$ -periodic perturbation to the steady state with the growth rate  $\lambda \in \mathbb{C}$ . If  $\text{Re}(\lambda) > 0$ , the perturbation  $f(\theta)e^{\lambda t}$  grows on the background of  $h(\theta)$  and induces instability of the steady-state solution in the time evolution of the model equation (1.1). Expressing  $h(\theta)$  from the third-order equation (2.1), we can rewrite the spectral problem (3.1) in the equivalent form,

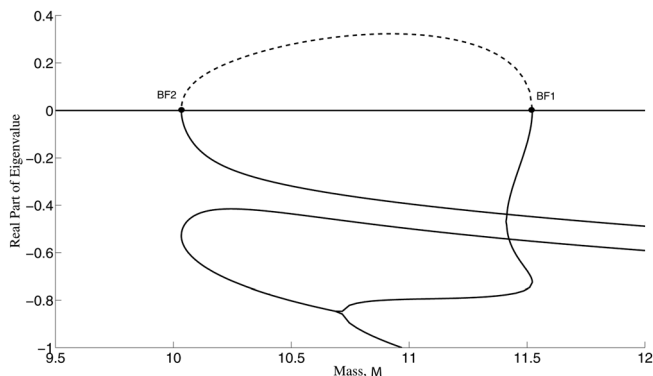


FIG. 5. The real part of the smallest eigenvalues  $\lambda$  of the spectral problem (3.1) for  $\epsilon = 0.001$ .

$$L f = \lambda f, \quad L = \frac{\partial}{\partial \theta} \left[ \frac{2h - 3Q}{h} - \frac{1}{3} \epsilon h^3 \left( \frac{\partial}{\partial \theta} + \frac{\partial^3}{\partial \theta^3} \right) \right]. \quad (3.2)$$

Note that there is always a zero eigenvalue in the spectral problem (3.2). Indeed,  $f_0 = \frac{\partial h}{\partial Q}$  is an eigenfunction for  $\lambda = 0$ , because  $Q$  is a free parameter of the steady state solution  $h$ . The zero eigenvalue corresponds physically to the fact that the steady-state solutions are represented by the one-parameter smooth curve on the mass–flux diagram.

We will now show that the zero eigenvalue is simple. First, since the Jacobian operator in the iteration algorithm was found to be invertible, the operator  $L_0$  is invertible, where

$$L_0 = \frac{2h - 3Q}{h} - \frac{1}{3} \epsilon h^3 \left( \frac{\partial}{\partial \theta} + \frac{\partial^3}{\partial \theta^3} \right).$$

Since  $L = \partial_\theta L_0$  and  $\partial_\theta$  has a one-dimensional kernel, the operator  $L$  has at most one eigenfunction in the kernel, which is  $f_0 = \frac{\partial h}{\partial Q}$ .

Next, we consider the adjoint spectral problem

$$L^* g = \lambda g, \quad L^* = \left[ \frac{3Q - 2h}{h} - \frac{1}{3} \epsilon \left( \frac{\partial}{\partial \theta} + \frac{\partial^3}{\partial \theta^3} \right) h^3 \right] \frac{\partial}{\partial \theta}. \quad (3.3)$$

It is clear that  $g_0 = 1$  is the adjoint eigenfunction for  $\lambda = 0$  and that

$$\langle g_0, f_0 \rangle = \frac{1}{2\pi} \int_{-\pi}^{\pi} \frac{\partial h}{\partial Q} d\theta = \frac{dM}{dQ}$$

is nonzero at all values of  $Q$  but the bifurcation points BF1 and BF2. By Fredholm’s theory for isolated eigenvalues, this fact implies that  $\lambda = 0$  is a simple eigenvalue for all values of  $Q$  but the bifurcation points BF1 and BF2.

TABLE I. Smallest nonzero eigenvalues of the spectral problem (3.1) for  $\epsilon = 0.001$  and  $M = 10.5$ .

Solution branch	Real $\lambda$	Complex $\lambda$
S1, $Q = 0.6601$	-0.32	$-0.44 \pm i0.79, -0.72 \pm i1.50$
S2, $Q = 0.6652$	-1.34	$-0.75 \pm i0.44, -1.31 \pm i0.97$
S3, $Q = 0.6686$	0.28	$-0.80 \pm i0.11, -1.18 \pm i1.07$

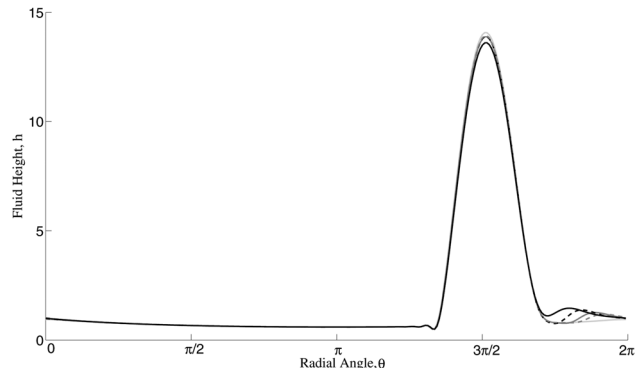
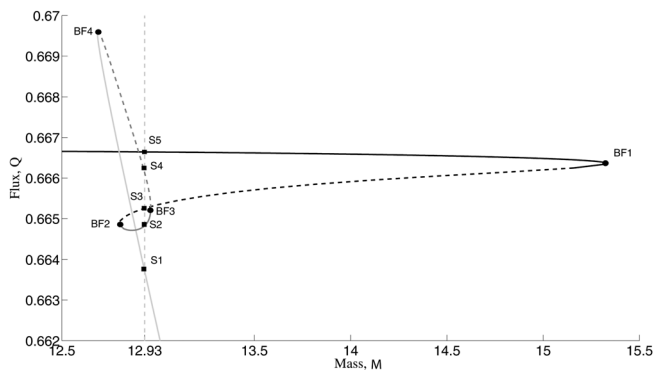


FIG. 6. (Top) A segment of the mass-flux diagram for  $\epsilon = 0.00039$ . Five branches are indicated between four bifurcation points (labeled BF1, BF2, BF3, and BF4 and shown by circles). The five branches are shown by solid light gray line (S1), solid dark gray line (S2), dashed line (S3), dashed gray line (S4), and solid black line (S5). The dashed gray line shows the value of mass  $M = 12.93$ . (Bottom) Five steady state solutions with  $M = 12.93$  and  $\epsilon = 0.00039$ : S1 (solid light gray line,  $Q = 0.6638$ ), S2 (solid dark gray line,  $Q = 0.6648$ ), S3 (dashed line,  $Q = 0.6653$ ), S4 (dashed gray line,  $Q = 0.6661$ ), S5 (solid black line,  $Q = 0.6666$ ).

We use a numerical method based on building a matrix representation of the differential operator  $L$  acting on  $f$ . To do so, we discretize the space and approximate the derivatives using the Fourier spectral method. The eigenvalue problem is then solved using the MATLAB function *eig*.

The real part of the smallest eigenvalues  $\lambda$  of the spectral problem (3.1) is shown in Figure 5 for  $\epsilon = 0.001$ . All other eigenvalues have larger negative real parts. Between the two bifurcation points BF1 and BF2, one eigenvalue

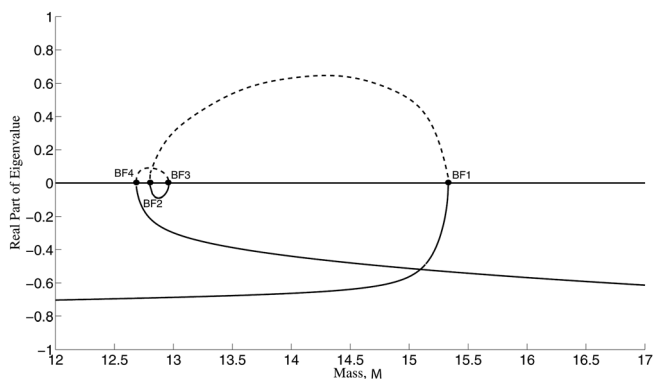


FIG. 7. The real part of the smallest eigenvalues  $\lambda$  of the spectral problem (3.1) for  $\epsilon = 0.00039$ .

TABLE II. Smallest nonzero eigenvalues of the spectral problem (3.1) for  $\epsilon = 0.00039$  and  $M = 12.93$ .

Branch	Real $\lambda$	Complex $\lambda$
S1, $Q = 0.6638$	-0.28, -3.76	$-0.42 \pm i0.70$ , $-0.65 \pm i1.41$ , $-0.90 \pm i2.25$
S2, $Q = 0.6648$	-0.07, -0.65	$-1.06 \pm i0.82$ , $-1.33 \pm i1.82$ , $-1.62 \pm i2.86$
S3, $Q = 0.6653$	0.30, -0.81	$-1.17 \pm i0.55$ , $-1.50 \pm i1.56$ , $-1.84 \pm i2.68$
S4, $Q = 0.6661$	0.05, -0.69	$-1.03 \pm i0.96$ , $-1.25 \pm i1.94$ , $-1.52 \pm i2.94$
S5, $Q = 0.6666$	-0.69, -2.57	$-1.33 \pm i0.46$ , $-1.54 \pm i1.46$ , $-2.31 \pm i1.32$

crosses zero and becomes unstable, revealing a saddle-node bifurcation at points BF1 and BF2. Branch S3 (between BF1 and BF2) is unstable with exactly one real positive eigenvalue  $\lambda$ . Other two branches S1 and S2 are stable with all but one zero eigenvalue having negative real parts. It follows from Figure 4 (bottom) that the unstable steady-state solution at branch S3 is squeezed between the stable solutions at branches S1 and S2. Small perturbations of the middle tail of the unstable solution are expected to grow towards the upper or lower tails of the other two stable solutions. Particular values of the smallest eigenvalues  $\lambda$  for branches S1, S2, and S3 are given in Table I.

Figure 6 (top) shows the mass-flux diagram for  $\epsilon = 0.00039$  with two loops. We can identify five solution branches (labeled as S1, S2, S3, S4, and S5) connected at four bifurcation points (labeled as BF1, BF2, BF3, and BF4). For  $M = 12.93$ , we compute the solution profiles and show them in Figure 6 (bottom). Although similar in their shapes, the five steady state solutions are clearly distinct. Properties of these solutions resemble those in Figure 4. In particular, multiple steady states exist for a fixed mass  $M$  and  $\epsilon$  and can be identified by their flux values  $Q$ . The five steady-state solutions are almost identical with the most visible deviation in their tails and peak heights.

Although the five steady-state solutions exist mathematically, whether or not they could exist physically depends on their stability. The real part of the smallest eigenvalues  $\lambda$  of the spectral problem (3.1) is shown in Figure 7 for  $\epsilon = 0.00039$ . All other eigenvalues have larger negative real parts. Between the bifurcation points BF1 and BF2, BF2 and BF3, BF3 and BF4, one eigenvalue crosses zero, revealing four saddle-node bifurcations at these points. Branch S3 (between BF1 and BF2) is unstable with exactly one real positive eigenvalue  $\lambda$ . Branch S4 between BF3 and BF4 is also unstable with exactly one real positive eigenvalue. Other three branches S1, S2, and S5 are stable with all but one zero eigenvalue having negative real parts. Again, we point readers to Figure 6 (bottom) that shows how tails of unstable solutions S3 and S4 are located in between the tails of stable solutions S1, S2, and S5. Particular values of the smallest eigenvalues  $\lambda$  for branches S1, S2, S3, S4, and S5 are given in Table II.

#### IV. CONCLUSION

We have explored the structure of steady-state solutions of the model for thin films in a rotating cylinder in the limit of small surface tension. We showed that increasing shocks persist under small surface tension. These shocks were then visualized on the mass-flux diagram by using numerical discretizations on a uniform grid. We have found loops of so-

lution branches on the mass-flux diagram and have shown numerically that the number of loops increases and their location moves to infinity on the mass-flux diagram as the surface tension decreases to zero.

We conclude by listing a number of open questions. First, it is suggested by the numerical computations that the number of solution branches goes to infinity as  $\epsilon \rightarrow 0$  but computations become difficult and unreachable for  $\epsilon < 10^{-5}$ . Second, the steady states are expected to persist with respect to small inclinations of the cylinder,<sup>33</sup> but we do not include inclined cylinders in this work. Finally, numerical discretizations on the adaptive (variable) grid can be developed further to resolve better the steady states near the shock location.

#### ACKNOWLEDGMENTS

This work was carried out during the Fields-MITACS Undergraduate Summer Research Program in Summer 2010. The authors thank A. Kulyk (Kharkov National Technical University) for collaborations during this program.

<sup>1</sup>L. W. Schwartz and D. E. Weidner, "Modeling of coating flows on curved surfaces," *J. Eng. Mech.* **29**, 91 (1995).

<sup>2</sup>O. E. Jensen, "The thin liquid lining of a weakly curved cylindrical tube," *J. Fluid Mech.* **331**, 373 (1997).

<sup>3</sup>A. E. Hosoi and L. Mahadevan, "Axial instability of a free-surface front in a partially filled horizontal rotating cylinder," *Phys. Fluids* **11**, 97 (1999).

<sup>4</sup>J. Ashmore, A. E. Hosoi, and H. A. Stone, "The effect of surface tension on rimming flows in a partially filled rotating cylinder," *J. Fluid Mech.* **479**, 65 (2003).

<sup>5</sup>P. L. Evans, L. W. Schwartz, and R. V. Roy, "Steady and unsteady solutions for coating flow on a rotating horizontal cylinder: Two-dimensional theoretical and numerical modeling," *Phys. Fluids* **16**, 2742 (2004).

<sup>6</sup>E. B. Hansen and M. A. Kelmanson, "Steady, viscous, free-surface flow on a rotating cylinder," *J. Fluid Mech.* **272**, 91 (1994).

<sup>7</sup>S. T. Thoroddsen and L. Mahadevan, "Experimental study of coating flows in a partially-filled horizontally rotating cylinder," *Exp. Fluids* **23**, 1 (1997).

<sup>8</sup>B. R. Duffy and S. K. Wilson, "Thin film and curtain flows on the outside of a horizontal rotating cylinder," *J. Fluid Mech.* **394**, 29 (1999).

<sup>9</sup>D. E. Weidner, L. W. Schwartz, and M. H. Eres, "Simulation of coating layer evolution and drop formation on horizontal cylinders," *J. Colloid Interface Sci.* **187**, 243 (1997).

<sup>10</sup>U. Thiele, "On the depinning of a drop of partially wetting liquid on a rotating cylinder," *J. Fluid Mech.* **671**, 121 (2011).

<sup>11</sup>H. K. Moffatt, "Behavior of a viscous film on outer surface of a rotating cylinder," *J. de Mecanique* **16**, 651 (1977).

<sup>12</sup>V. V. Pukhnachov, "Motion of a liquid film on the surface of a rotating cylinder in a gravitational field," *J. Appl. Mech. Tech. Phys.* **18**, 344 (1977).

<sup>13</sup>S. K. Wilson, R. Hunt, and B. R. Duffy, "On the critical solutions in coating and rimming flow on a uniformly rotating horizontal cylinder," *Q. J. Mech. Appl. Math.* **55**, 357 (2002).

<sup>14</sup>E. J. Hinch and M. A. Kelmanson, "On the decay and drift of free-surface perturbations in viscous thin-film flow exterior to a rotating cylinder," *Proc. R. Soc. London Ser. A* **459**, 1193 (2003).

- <sup>15</sup>A. Acrivos and B. Jin, "Rimming flows within a rotating horizontal cylinder: Asymptotic analysis of the thin-film lubrication equations and stability of their solutions," *J. Eng. Math.* **50**, 99 (2004).
- <sup>16</sup>C. J. Noakes, J. R. King, and D. S. Riley, "On three-dimensional stability of a uniform, rigidly rotating film on a rotating cylinder," *Q. J. Mech. Appl. Math.* **58**, 229 (2005).
- <sup>17</sup>C. J. Noakes, J. R. King, and D. S. Riley, "On the development of rational approximations incorporating inertial effects in coating and rimming flows: A multiple-scales approach," *Q. J. Mech. Appl. Math.* **59**, 163 (2006).
- <sup>18</sup>C. H. Toghiani, S. K. Wilson, and B. R. Duffy, "On the approach to the critical solution in leading order thin-film coating and rimming flow," *Appl. Math. Lett.* **22**, 882 (2009).
- <sup>19</sup>K. Pougatch and I. Frigaard, "Thin film flow on the inside surface of a horizontally rotating cylinder: Steady state solutions and their stability," *Phys. Fluids* **23**, 022102 (2011).
- <sup>20</sup>M. Tirumkudulu and A. Acrivos, "Coating flows within a rotating horizontal cylinder: Lubrication analysis, numerical computations, and experimental measurements," *Phys. Fluids* **13**, 14 (2001).
- <sup>21</sup>P. J. Chen, Y. T. Tsai, T. J. Liu, and P. Y. Wu, "Low volume fraction rimming flow in a rotating horizontal cylinder," *Phys. Fluids* **19**, 128107 (2007).
- <sup>22</sup>R. Hunt, "Numerical solution of the free-surface viscous flow on a horizontal rotating elliptical cylinder," *Numer. Methods Partial Differ. Equ.* **24**, 1094 (2008).
- <sup>23</sup>S. B. G. O'Brien, "Linear stability of rimming flow," *Q. Appl. Math.* **60**, 201 (2002).
- <sup>24</sup>R. E. Johnson, "Steady state coating flows inside a rotating horizontal cylinder," *J. Fluid Mech.* **190**, 321 (1988).
- <sup>25</sup>T. B. Benjamin, W. G. Pritchard, and S. J. Tavener, "Steady and unsteady flows of a highly viscous fluid inside a rotating horizontal cylinder," Penn State University Report No. AM 122, 1993.
- <sup>26</sup>S. D. R. Wilson and J. Williams, "The flow of a liquid film on the inside of a rotating cylinder," *Phys. Fluids* **9**, 2184 (1997).
- <sup>27</sup>S. B. G. O'Brien and E. G. Gath, "The location of a shock in rimming flow," *Phys. Fluids* **10**, 1040 (1998).
- <sup>28</sup>E. S. Benilov, M. S. Benilov, and S. B. G. O'Brien, "Existence and stability of regularized shock solutions, with applications to rimming flows," *J. Eng. Math.* **63**, 197 (2009).
- <sup>29</sup>V. V. Pukhnachov, "Asymptotic solution of the rotating film problem," *Izv. Vyssh. Uchebn. Zaved. Severo-Kavkaz. Reg. Estestv. Nauk, Mathematics and Continuum Mechanics (a special issue)*, 191 (2004).
- <sup>30</sup>E. A. Karabut, "Two regimes of liquid film flow on a rotating cylinder," *J. Appl. Mech. Tech. Phys.* **48**, 55 (2007).
- <sup>31</sup>E. S. Benilov, M. S. Benilov, and N. Kopteva, "Steady rimming flows with surface tension," *J. Fluid Mech.* **597**, 91 (2008).
- <sup>32</sup>B. R. Duffy and S. K. Wilson, "A third-order differential equation arising in thin-film flows and relevant to Tanner's law," *Appl. Math. Lett.* **10**, 63 (1997).
- <sup>33</sup>S. V. Alekseenko, P. I. Geshev, and P. A. Kuibin, "Free-boundary fluid flow on an inclined cylinder," *Sov. Phys. Dokl.* **42**, 269 (1997).